Available Online: 10 June 2025 DOI: 10.54254/2977-3903/2025.23781

Study on rare-earth element-doped copper halides

Haifeng Chen

School of Integrated Circuits, Dalian University of Technology, Dalian, China

15904180909@139.com

Abstract. Environmentally friendly lead-free metal halide scintillators have attracted significant research interest in recent years in the field of radiation detection due to their low toxicity and outstanding radioluminescent properties. However, enhancing the luminescence performance of lead-free metal halide scintillators and fabricating thin films that integrate high light output, high spatial resolution, and excellent compatibility with photodetectors remain major challenges. To address these issues, this study employs $Cs_3Cu_2I_5$ as the scintillating material and introduces Terbium (Tb) doping to tune its emission to match current photodetectors. A high-refractive-index flexible UV-curable adhesive, NOA170F, is used as the matrix to synthesize a $Cs_3Cu_2I_5$: Tb scintillating thin film featuring a large Stokes shift, high luminescence intensity, low cost, environmental friendliness, and good stability. The luminescence mechanism and X-ray scintillation properties of the film are also investigated.

Keywords: X-ray imaging, scintillator, Tb doping

1. Introduction

In recent years, metal halide materials have attracted significant attention as scintillators due to their high energy conversion efficiency, tunable wavelength and response time, and low fabrication cost. They have become star materials in the field of optoelectronic semiconductors. X-ray scintillation imaging is a key technology in medical diagnostics, industry, and security inspection. Indirect X-ray detection using scintillators converts high-energy X-ray radiation into low-energy ultraviolet/visible photons, which can be detected by conventional photodetectors to obtain digitized X-ray images [1, 2]. Scintillator-based X-ray imaging systems have become mainstream in the current market due to their relatively simple components and operational stability. However, traditional halide perovskite materials contain heavy metal lead (Pb) and toxic organic components, which severely limit their practical commercial application [3-5]. As a result, the synthesis and optical properties of lead-free halide perovskites have drawn increasing research interest. A new type of inorganic perovskite nanocrystal material, $Cs_3Cu_2I_5$, has emerged as a promising candidate due to its non-toxic nature and high stability, attracting considerable attention from researchers [6-8].

Colloidal scintillators composed of $Cs_3Cu_2I_5$ exhibit efficient radioluminescence and are promising for low-cost radiography and flexible X-ray imaging applications, and have received growing interest in recent years. However, there is still substantial room for improvement in the practical application of $Cs_3Cu_2I_5$ perovskite-based thin films:

First, the uniformity of transparent films with efficient radioluminescence is key to achieving high-resolution X-ray imaging. A major factor affecting film transparency is strong light scattering. Perovskite particles have a higher refractive index than typical organic and inorganic matrix materials, but how to efficiently extract light from scintillator particles within a polymer matrix with minimal loss remains a critical issue. Therefore, utilizing a semi-solid matrix with a refractive index close to that of the scintillator particles may offer a new approach to achieving higher light output.

Second, although $Cs_3Cu_2I_5$ has been extensively studied as a representative scintillator due to its excellent scintillation properties, its emission spectrum in the blue-light region aligns well only with the peak Quantum Efficiency (QE) of Photomultiplier Tubes (PMTs). In contrast, it is significantly mismatched with the peak QE of typical silicon-based photodetectors used in X-ray imaging, resulting in low scintillation photon collection efficiency. In follow-up studies, metal ion doping has demonstrated significant advantages in enhancing the light yield of scintillators, and spectral emission tuning can be achieved through doping strategies, structural adjustments, and compositional modulation. Rare-earth elements, in particular, have shown great potential in improving the optical performance of materials, effectively enhancing the luminescence efficiency and stability of scintillating films. However, despite their theoretical ability to deliver optimal luminescence performance, the practical application of rare-earth elements faces a series of challenges [9].

Copyright: © 2025 by the authors. Submitted for possible open access publication under the terms and conditions of the Creative Commons Attribution (CC BY) license (https://creativecommons.org/licenses/by/4.0/).

The high cost of rare-earth elements generally limits their feasibility for large-scale applications. Moreover, certain rare-earth elements exhibit a degree of toxicity, posing potential environmental and human health risks. This necessitates special attention to safety and environmental considerations during material production and usage. Therefore, there is an urgent need to develop a novel in-situ fabrication strategy that not only effectively reduces production costs but also improves the overall performance of $Cs_3Cu_2I_5$ nanocomposite scintillating films without compromising luminescence efficiency. Such a strategy would open broader prospects for future research and applications, driving the advancement of scintillation materials in a wide range of optoelectronic devices.

2. Preparation methods for polycrystals and scintillation screens

2.1. Preparation of $Cs_3Cu_2I_5$: Tb polycrystals

In this study, a scintillator polycrystal was synthesized using an in situ growth method, with the procedure detailed as follows:

To prepare the $Cs_3Cu_2I_5$: Tb polycrystal, copper (I) iodide (CuI, 98%, Aladdin), cesium iodide (CsI, 98%, Aladdin), and N, N-dimethylformamide (DMF, 99.9%, Aladdin) were used. First, $TbCl_3 \cdot 6H_2O$ was placed in a heating furnace and heated to 100 °C for 20 minutes to evaporate the water content, yielding a dried polycrystalline powder. Next, 1.5236 g (8 mmol) of CuI and 3.1178 g (12 mmol) of CsI were precisely weighed and added to a glass vial containing 5 mL of DMF, followed by 100 μL of hypophosphorous acid. The mixture was stirred at 60 °C on a magnetic hotplate for 30 minutes until fully dissolved into a transparent solution, forming the precursor solution. The Tb element was doped into the precursor solution at a specific molar ratio. Subsequently, the precursor solution was added dropwise into 5 mL of isopropanol as an anti-solvent. The transparent solution and isopropanol were mixed at a 1:5 ratio and stirred vigorously. The resulting mixture was centrifuged at 10,000 rpm for 5 minutes, leading to the precipitation of $Cs_3Cu_2I_5$: Tb polycrystals. The supernatant was discarded, and the precipitate was vacuum-dried at room temperature overnight. The resulting solid was ground thoroughly in an agate mortar to obtain the polycrystalline powder, as shown in Figure 1.

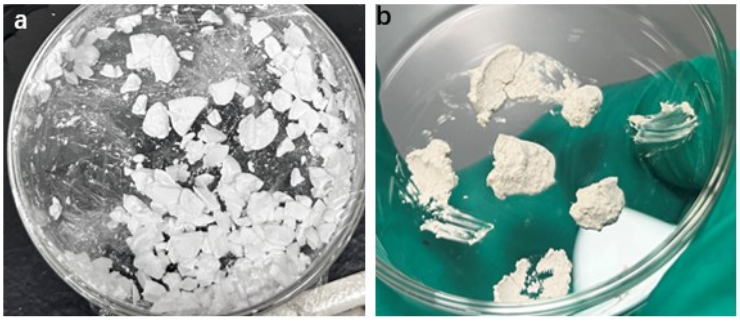

Figure 1. (a) $Cs_3Cu_2I_5$ polycrystalline powder and (b) $Cs_3Cu_2I_5$: Tb polycrystalline powder

2.2. Preparation of $Cs_3Cu_2I_5$: Tb scintillation film

The preparation process of $Cs_3Cu_2I_5$ thin films is illustrated in Figure 2. First, 2 g of $Cs_3Cu_2I_5$ polycrystalline powder (dried overnight in vacuum) was mixed with 0.6 g of carrier material and an appropriate amount of ethyl acetate. The mixture was stirred at 80 °C for 1 hour and collected as the precursor solution. This solution was then used to fabricate thin films by blade-coating onto a glass substrate that had been ultrasonically cleaned with acetone, ethanol, and deionized water for 30 minutes. The coated film was annealed on a hot plate at 75 °C. After the solvent fully evaporated, a $Cs_3Cu_2I_5$ scintillation film of a certain thickness was formed. Upon UV excitation, the fully crystallized film exhibited uniform blue luminescence and could be peeled off from the glass substrate. It is important to note that hotplate annealing can result in pinholes on the surface of the $Cs_3Cu_2I_5$ polycrystalline film after solvent evaporation, compromising film quality. Therefore, a constant-temperature oven annealing method was employed to allow faster and more uniform solvent evaporation, resulting in high-quality films. This improvement is attributed to the airflow in the oven, which promotes the rapid and even dispersion of DMF within the film, enabling simultaneous drying from the inside out and synchronous crystal growth of $Cs_3Cu_2I_5$ throughout the entire film.

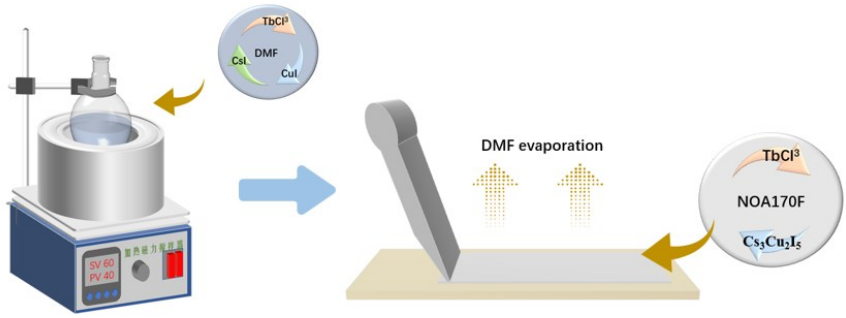

Figure 2. Preparation process of $Cs_3Cu_2I_5$: Tb film

When NOA170F was used as the carrier material, the preformed film was cured under nitrogen for 1 hour, as shown in Figure 3. Simultaneously, a 365 nm UV curing lamp with a power of 10 W was used for photopolymerization. After complete curing and solidification, the film could be peeled off.

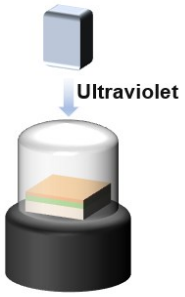

Figure 3. The carrier is cured as a NOA170F film

3. Phase analysis

3.1. Crystal structure of $Cs_3Cu_2I_5$: Tb

Due to the limited number of studies on Cu-based halide scintillators, there are no standard parameters such as PDF cards available for reference. Therefore, this study compares the obtained results with the information reported in relevant literature. While $Cs_3Cu_2I_5$ has been documented, no prior literature has reported the doping of $Cs_3Cu_2I_5$ with Tb. The experimental data presented here are provided for reference in future research.

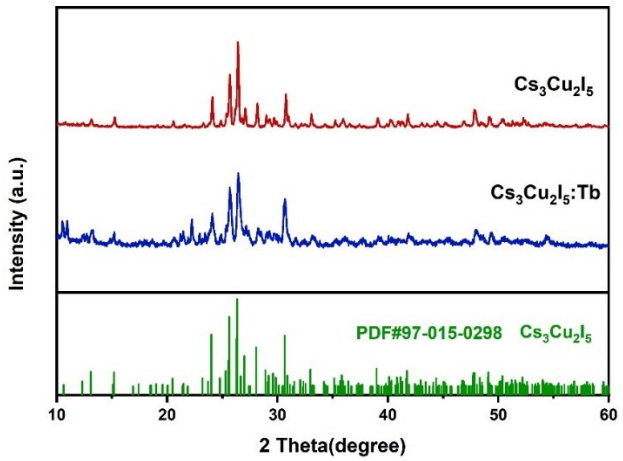

Figure 4. XRD patterns of (a) $Cs_3Cu_2I_5$ and (b) $Cs_3Cu_2I_5$: Tb

As shown in Figure 4, in the XRD pattern of $Cs_3Cu_2I_5$: Tb, the positions of the diffraction peaks correspond to the interplanar spacings of specific crystal planes. When compared with the standard XRD pattern of pure-phase $Cs_3Cu_2I_5$, a noticeable shift in the peak positions is observed, indicating the presence of Tb in $Cs_3Cu_2I_5$: Tb. This shift suggests that doping with Tb alters the lattice constants. The reason lies in the difference in ionic radii between Tb^{3+} and the substituted Cu^+ ions, which leads to lattice distortion and an increase in the interplanar spacing. According to Bragg's law, an increase in the interplanar spacing results in a decrease in the diffraction angle θ, which in turn causes the shift in the diffraction peak positions.

3.2. X-ray Photoelectron Spectroscopy (XPS)

The XPS spectra of both $Cs_3Cu_2I_5$ and $Cs_3Cu_2I_5$ doped with the rare earth element Tb are shown in Figure 5.

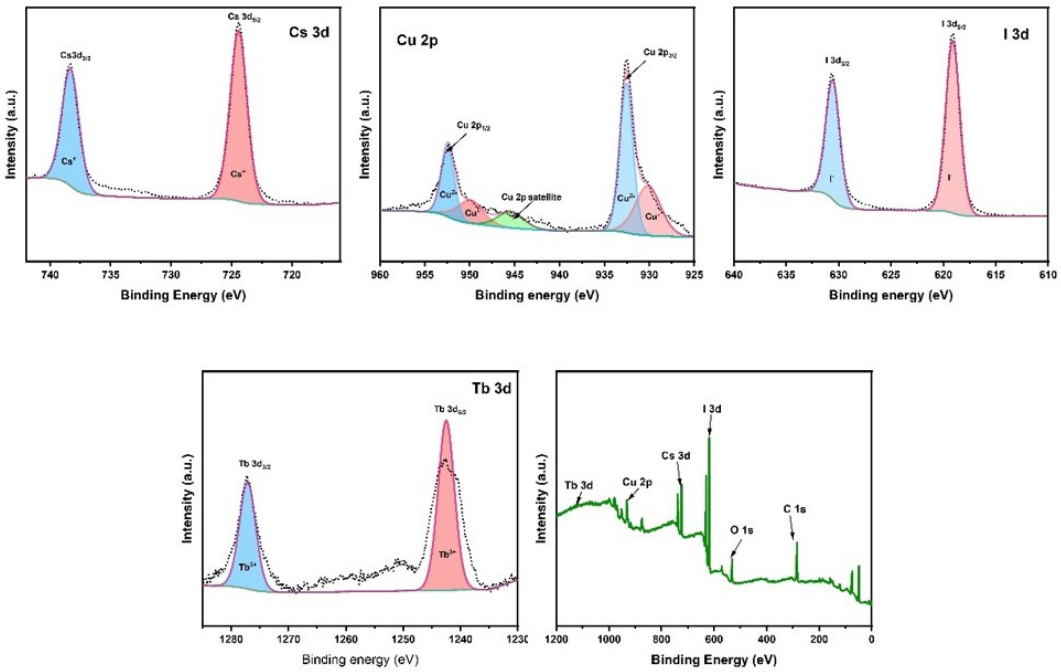

Figure 5. XPS spectra of $Cs_3Cu_2I_5$: Tb: (a) Cu 2p (b) I 3d (c) Cs 3d (d) Tb 3d (e) full spectrum

XPS analysis was used to further investigate the valence states of the elements in the material. As shown, the full spectra of both $Cs_3Cu_2I_5$ and $Cs_3Cu_2I_5$: Tb display characteristic peaks. High-resolution fitting reveals that in the Cu 2p spectrum, two distinct spin-orbit split peaks of copper's 2p orbital are observed at 932.7 eV and 952.6 eV, with an energy separation of 19.9 eV. These correspond to Cu $2p_{3/2}$ and Cu $2p_{1/2}$, respectively, and match the binding energy of Cu^+ in $Cs_3Cu_2I_5$. In the I 3d spectrum, the doublet peaks at 619.3 eV and 630.8 eV correspond to I $3d_{5/2}$ and I $3d_{3/2}$, with a separation of 11.5 eV. These values are consistent with the standard binding energies of iodide (I^-). In the Cs 3d spectrum, the peaks at 724.6 eV and 738.6 eV represent Cs $3d_{5/2}$ and Cs $3d_{3/2}$, respectively, with a separation of 14 eV. These values correspond to Cs^+, indicating that Cs exists in a single valence state. For the Tb spectrum in $Cs_3Cu_2I_5$: Tb, the peaks at 1230.5 eV and 1240.6 eV correspond to Tb $3d_{3/2}$ and Tb $3d_{5/2}$, respectively. The observed splitting of 10.1 eV is characteristic of Tb^{3+}, and the peak positions align well with known values for Tb^{3+}. Tb^{3+} has a higher positive charge than Tb^{2+}, resulting in greater charge density and stronger attraction to surrounding electrons. This leads to higher binding energies for core electrons. As higher binding energy correlates with a shift of XPS peaks toward higher energy values, the absence of any noticeable shift toward lower binding energies suggests that Tb predominantly exists in the trivalent state, with no evidence of metallic or other valence states. Since XPS is a surface-sensitive technique and surface oxidation is common, the Cu 2p spectrum was examined for any signs of Cu^{2+} peaks. None were found, indicating that Cu^+ is relatively stable and not easily oxidized, further supporting the material's chemical stability. The above analysis confirms the presence of Cs, Cu, I, and Tb in the material, with Tb acting as a dopant and existing in the trivalent state.

4. Fluorescence characterization

After confirming that the material possesses a high-purity single phase, the optical properties of the material were further investigated. The optical performance of Tb-doped $Cs_3Cu_2I_5$ polycrystalline materials was examined, and the optimal doping

concentration was selected for the fabrication of scintillator screens. $Cs_3Cu_2I_5$: Tb (15%) was taken as a representative sample to analyze the self-trapped exciton emission behavior of this material.

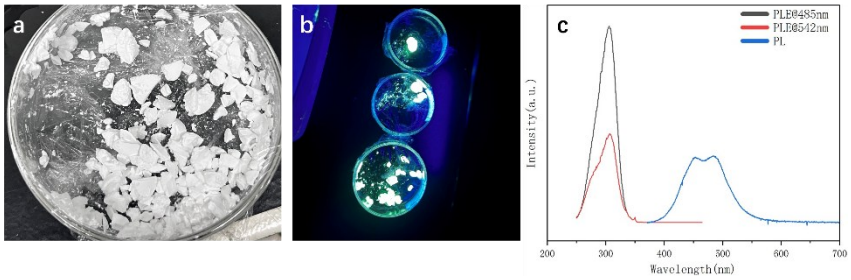

Figure 6. (a) Photographs of $Cs_3Cu_2I_5$: Tb polycrystalline under ambient light and ultraviolet light (254 nm); (b) Emission and excitation spectra

Emission spectra were first tested, as shown in Figure 6. The photographs reveal that $Cs_3Cu_2I_5$: Tb polycrystals appear pure white under ambient light, indicating negligible absorption in the visible range. Under UV excitation at 254 nm, the material emits a distinct blue-green light. Figure 6(c) presents the excitation spectrum of the Tb-doped $Cs_3Cu_2I_5$ polycrystalline material. The results show that $Cs_3Cu_2I_5$: Tb exhibits two prominent emission bands at 485 nm and 542 nm. The PL emission spectrum spans the entire visible range, with a strong and broad emission peak between 450–550 nm, indicating robust luminescence in this band and corresponding to the observed blue-green emission. The emission at 485 nm is similar to that of undoped $Cs_3Cu_2I_5$, which is attributed to self-trapped exciton luminescence, while the strongest characteristic emission peak at 542 nm corresponds to the $^5D_4 \rightarrow {}^7F_5$ transition, a hallmark of Tb^{3+}.

Using a dual-channel photoluminescence excitation spectrum analysis system, the energy level transition mechanisms of the emission bands at 485 nm (blue-green light) and 542 nm (yellow-green light) were studied in detail. As shown in the figure, both emission channels exhibit a broadened excitation band centered at 310 ± 2 nm, with highly consistent spectral profiles in the 295–325 nm range. This suggests that both emissions share a common matrix-activator charge transfer excitation pathway.

Through Jablonski diagram analysis, the corresponding Stokes shifts were calculated as $\Delta\lambda\_S$ (485) = 175 nm (ΔE = 1.72 eV) and $\Delta\lambda\_S$(542) = 232 nm (ΔE = 2.01 eV), significantly exceeding those of typical inorganic scintillators. According to the Beer-Lambert law, the self-absorption coefficient α_self can be reduced to the order of 10^{-3} cm^{-1}, approximately two orders of magnitude lower than that of conventional scintillators. These findings provide critical evidence for subsequent analysis of potential energy transfer pathways and excitation relaxation mechanisms in $Cs_3Cu_2I_5$: Tb.

4.1. Fluorescence spectra of $Cs_3Cu_2I_5$: Tb

As shown in Figure 7, the PL spectra of $Cs_3Cu_2I_5$: Tb polycrystals with different doping concentrations under 254 nm UV excitation reveal that in the absence of Tb doping, the main emission peak appears between 445 nm and 540 nm, with the strongest emission at 445 nm, characteristic of the self-trapped exciton emission of pure-phase $Cs_3Cu_2I_5$. Upon Tb doping, as the concentration increases from 1% to 20%, the luminescence intensity increases significantly, indicating an energy transfer mechanism within the Tb-doped $Cs_3Cu_2I_5$ system. The excitation energy is gradually transferred to Tb^{3+} ions, and the strongest emission peak shifts to around 500 nm as doping increases, with bright green light observed. Additionally, a characteristic emission peak of Tb^{3+} ions emerges around 543 nm and intensifies with higher doping levels. This enhancement corresponds to the green emission associated with the $^5D_4 \rightarrow {}^7F_j$ transition of Tb^{3+} ions. Generally, the $^5D_4 \rightarrow {}^7F_j$ transition is a signature of Tb^{3+} ions. The luminescence of Tb^{3+} primarily originates from electronic transitions between its 4f–4f energy levels, especially the series of transitions from the excited state $^5D_4$ to the ground multiplet ^7F_j. Among these, the $^5D_4 \rightarrow {}^7F_5$ transition corresponds to the strongest emission peak at 543 nm, which lies in the visible green region and finds broad application in display materials. This emission results from an electric dipole transition. Although 4f–4f transitions are forbidden in free ions, the symmetry breaking in crystals renders them partially allowed, resulting in strong luminescence. The spectral properties of this transition serve as a sensitive and stable optical probe for investigating energy transfer behavior in Tb^{3+}-doped materials.

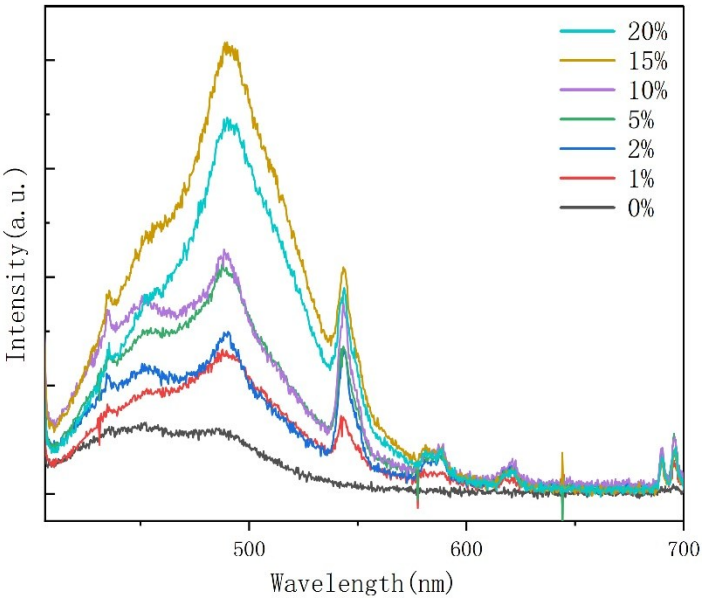

Figure 7. PL spectra of $Cs_3Cu_2I_5$: Tb polycrystalline at various concentrations under ultraviolet light (254 nm)

4.2. Fluorescence spectrum of $Cs_3Cu_2I_5$: Tb scintillation screen

As shown in Figure 8, the Photoluminescence (PL) spectra of $Cs_3Cu_2I_5$: Tb@NOA170F (15%) scintillator films with different thicknesses—220 μm, 310 μm, 330 μm, and 340 μm—are presented. By comparing the PL spectra of the films with varying thicknesses, it is evident that, since the scintillator polycrystalline powders are uniformly dispersed within the films, the loading of the scintillator powders varies with film thickness. Through repeated experiments with films of different thicknesses, it was found that the brightness of the scintillator films gradually increases with increasing thickness.

From the spectra, it can be observed that the PL emission intensity enhances progressively with the increase in film thickness. As the thickness increases from 220 μm to 340 μm, the emission intensity significantly improves. The PL intensity of the 220 μm film is relatively weak due to the lower absorption efficiency of the excitation light in thinner films. As a result, fewer Tb^{3+} ions are excited, leading to weaker emission. With increasing thickness, the penetration depth of the excitation light grows, allowing more Tb^{3+} ions to be excited and thus producing a stronger luminescent response. The emission intensity of the 340 μm film is nearly five times that of the 220 μm film. However, the emission intensity of the 340 μm film shows no significant increase compared to that of the 330 μm film, indicating that the enhancement trend is approaching saturation. This suggests that although thicker films can absorb more excitation light and activate more Tb^{3+} ions, the penetration of light becomes limited, especially in the inner layers of thicker films, where the absorption of excitation light diminishes. At this point, internal energy transfer and light scattering effects within the film slow the increase in emission intensity. Hence, further increasing film thickness may not effectively enhance luminescence performance, and oversizing the film can lead to saturation.

Regardless of whether the film is as thin as 220 μm or as thick as 340 μm, the emission peak remains within the same wavelength range, demonstrating stable luminescent characteristics. This emission peak stability indicates that the luminescence mechanism of the Tb^{3+}-doped material is not significantly affected by variations in film thickness.

Moreover, although increasing the film thickness notably improves emission intensity, there are still several challenges and difficulties in the fabrication process of $Cs_3Cu_2I_5$ scintillator films doped with Tb and based on NOA170F. For instance, manufacturing thicker films is more difficult, and precise control over film thickness requires sophisticated techniques and depends heavily on manual blade-coating experience. Additionally, the uniformity and crystallinity of the material may be constrained by the growth conditions of thicker films. One of the key factors affecting image quality is the uniform dispersion of scintillator polycrystalline powders in the carrier. Although ethyl acetate is currently added to assist dispersion in industrial practice, its effectiveness remains limited. Finally, the film formation process for NOA170F-based scintillator films must be carried out in a vacuum or nitrogen-filled protective environment and cured with UV light at a wavelength of 365 nm. Therefore, there is still room for improvement in the mass industrial fabrication of such scintillator films. In actual production, it is necessary to consider the film thickness, emission intensity, and other physical properties comprehensively to achieve optimal scintillation performance.

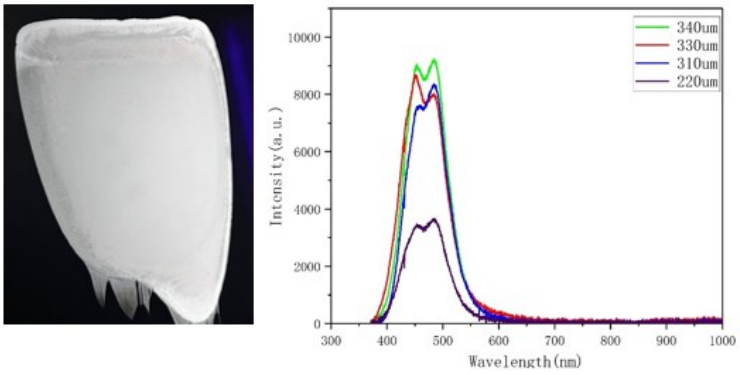

Figure 8. PL spectra of $Cs_3Cu_2I_5$: Tb@NOA170F (15%) scintillator films with different thicknesses and real image of the films

5. Imaging study of $Cs_3Cu_2I_5$: Tb scintillator screen

As demonstrated in the preceding sections, $Cs_3Cu_2I_5$ scintillator polycrystalline powder doped with rare earth element Tb exhibits characteristics such as high light yield, strong luminescence intensity, and a linear relationship with radiation energy, indicating its potential to serve as a high-performance scintillator. Consequently, this study developed a flexible $Cs_3Cu_2I_5$: Tb scintillator film featuring simple fabrication, high stability, excellent scintillation performance, and superior imaging resolution. In this section, a TPACI@NOA170F flexible scintillator film was fabricated using an insitu crystallization blade-coating method and evaluated using a laboratory-built X-ray imaging platform, demonstrating outstanding X-ray imaging performance. This work provides a promising approach for manufacturing high-resolution, flexible scintillator films.

Currently, no known industrial process uses NOA170F colloid as the host matrix for fabricating scintillator films. However, the preparation process resembles that of using PVDF as the film substrate. In 2016, Zhou et al. were the first to employ an in situ growth method to fabricate $MAPbBr_3$@PVDF composite films. The films were produced using a solvent casting–vacuum annealing method based on the non-solvent-induced phase separation mechanism. In the first stage, precursor molecules self-assemble: a 1.05:1 molar ratio of MABr/$PbBr_2$ and PVDF is co-dissolved in DMF, stirred magnetically at 800 rpm for four hours to obtain a stable colloidal solution with a zeta potential of +32 mV. This solution is then blade-coated onto an oxygen plasma-treated glass substrate to form a wet film.

The second stage involves controlling solvent evaporation kinetics: the wet film is transferred into a vacuum oven, where the DMF evaporation rate is modeled based on Fick's second law. Drying is terminated when the residual solvent concentration falls below 0.1 wt%, resulting in a perovskite precursor framework encapsulated by β-phase PVDF. The third stage consists of in situ lattice reconstruction: topochemical conversion of $MAPbBr_3$ is performed in a nitrogen atmosphere annealing furnace. XRD analysis shows cooperative orientation growth between the cubic-phase perovskite and the PVDF (200) crystal plane.

In contrast, the fabrication of the $Cs_3Cu_2I_5$: Tb@NOA170F composite film differs in the second stage. After obtaining a uniform precursor coating, the film is cured under a nitrogen atmosphere for one hour using a UV curing lamp (wavelength 365 nm, power 10 W). Once fully solidified, the film can be peeled off.

Following the preparation of the $Cs_3Cu_2I_5$: Tb@NOA170F scintillator film with a doping concentration of 15%, X-ray imaging was conducted (see Figure 9). The spatial resolution of a scintillator is defined as the number of line pairs resolvable per millimeter. A line pair refers to a pair of equal-width bright and dark stripes or periodically spaced light-dark lines. Spatial resolution quantifies the film's ability to resolve target details—the higher the resolution, the greater the detail discernibility.

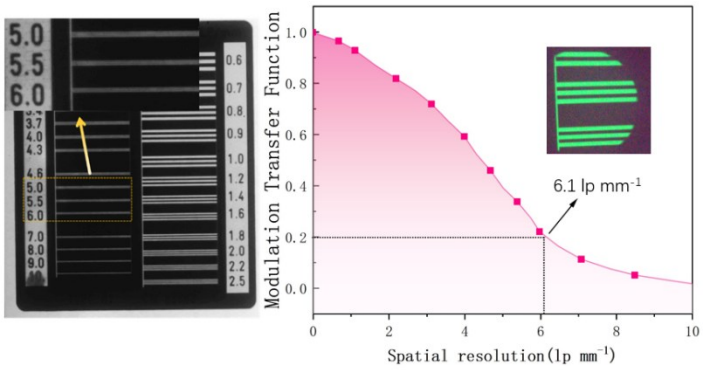

Figure 9. MTF curve of thin membrane

6. Conclusion

This study characterized the basic physical and luminescent properties of $Cs_3Cu_2I_5$ polycrystals doped with Tb and found that, compared to the pure-phase $Cs_3Cu_2I_5$, the doped material exhibits higher photoluminescence quantum yield and larger Stokes shift. Based on a doping concentration gradient, the optimal doping range for luminescence performance was determined, with a 15% doping level used as an example for STE luminescence analysis. Furthermore, the host matrix of the scintillator film was investigated and compared with commonly used matrices in the industry. The results show that NOA170F, as a film matrix, maximizes the luminescent performance of the scintillator film. The optimal doping ratio was established, and the resulting scintillator film exhibited excellent luminescent properties. It also demonstrated the capability for conformal X-ray imaging.

References

[1] Liu, J., Shabbir, B., & Wang, C. (2019). Flexible, printable soft-X-ray detectors based on all-inorganic perovskite quantum dots. *Advanced Materials*, *31*(30), 1901644.
[2] Sen, S., Tyagi, M., & Sharma, K. (2017). Organic-inorganic composite films based on Gd3Ga3Al2O12: Ce scintillator nanoparticles for X-ray imaging applications. *ACS Applied Materials & Interfaces*, *9*(42), 37310-37320.
[3] Lee, J. H., & Lee, J. W. (2022). Van der waals metal contacts for characterization and optoelectronic application of metal halide perovskite thin flms. *ACS Energy Letters*, *7*, 3780-3787.
[4] Qiao, L., Fang, W. H., & Prezhdo, O. V. (2022). Suppressing oxygen-induced deterioration of metal halide perovskites by alkaline earth metal doping: a quantum dynamics study. *Journal of the American Chemical Society*, *144*, 5543-5551.
[5] Zhao, F., Ren, A., &Li, P. (2022). Toward continuous-wave pumped metal halide perovskite lasers: strategies and challenges. *ACS Nano*, *16*, 7116-7143.
[6] Zhou, Y., Chen, J., &Bakr, O. M. (2021). Metal Halide Perovskites for X-ray Imaging Scintillators and Detectors. *ACS Energy Letter*s, *6*(2), 739-768.
[7] Wu, H., Ge, Y., &Niu, G. (2021). Metal Halide Perovskites for X-Ray Detection and Imaging. *Matter*, *4*(1), 144-163.
[8] Jana, A., Cho, S., &Patil, S. A. (2022). Perovskite: Scintillators, Direct Detectors, and X-ray Imagers. *Materials Today*, *55*, 110-136.
[9] Dunlap-Shohl, W. A., Zhou, Y., Padture, N. P., & Mitzi, D. B. (2019). *Chemical Review*s, *119*, 3193.